PHYSICAL REVIEW APPLIED **15,** 014006 (2021)

Understanding Dark Current-Voltage Characteristics in Metal-Halide Perovskite Single Crystals

Elisabeth A. Duijnstee,[1] Vincent M. Le Corre,[2] Michael B. Johnston,[1] L. Jan Anton Koster,[2,*]
Jongchul Lim,[1,3,†] and Henry J. Snaith[1,‡]

[1] *Clarendon Laboratory, University of Oxford, Parks Road, Oxford OX1 3PU, United Kingdom*
[2] *Zernike Institute for Advanced Materials, University of Groningen, Nijenborgh 4, Groningen 9747 AG, Netherlands*
[3] *Graduate School of Energy Science and Technology, Chungnam National University, 99 Daehak-ro, Yuseong-gu, Daejeon 34134, Republic of Korea*

(Received 17 September 2020; revised 26 November 2020; accepted 7 December 2020; published 6 January 2021)

Hybrid halide perovskites have great potential for application in optoelectronic devices. However, an understanding of some basic properties, such as charge-carrier transport, remains inconclusive, mainly due to the mixed ionic and electronic nature of these materials. Here, we perform temperature-dependent pulsed-voltage space-charge-limited current measurements to provide a detailed look into the electronic properties of methylammonium lead tribromide ($MAPbBr_3$) and methylammonium lead triiodide ($MAPbI_3$) single crystals. We show that the background carrier density in these crystals is orders of magnitude higher than that expected from thermally excited carriers from the valence band. We highlight the complexity of the system via a combination of experiments and drift-diffusion simulations and show that different factors, such as thermal injection from the electrodes, temperature-dependent mobility, and trap and ion density, influence the free-carrier concentration. We experimentally determine effective activation energies for conductivity of (349 ± 10) meV for $MAPbBr_3$ and (193 ± 12) meV for $MAPbI_3$, which includes the sum of all of these factors. We point out that fitting the dark current density-voltage curve with a drift-diffusion model allows for the extraction of intrinsic parameters, such as mobility and trap and ion density. From simulations, we determine a charge-carrier mobility of 12.9 cm^2/Vs, a trap density of 1.52×10^{13} cm^{-3}, and an ion density of 3.19×10^{12} cm^{-3} for $MAPbBr_3$ single crystals. Insights into charge-carrier transport in metal-halide perovskite single crystals will be beneficial for device optimization in various optoelectronic applications.

DOI: 10.1103/PhysRevApplied.15.014006

I. INTRODUCTION

Metal-halide perovskites are prospective candidates for facilitating not only third-generation solar-cell technologies [1–3], but also other applications, such as solid-state lasers [4,5], light-emitting diodes [6], and radiation detectors [7]. It is widely known that perovskites possess, apart from electronic conductivity, ionic conductivity, where mobile ions can shield the bulk material from externally applied biases [8–10]. In this regard, electronic charge-carrier dynamics can be strongly influenced by the existence of drifting and diffusing mobile ions, which makes the use of traditional electrical characterization techniques questionable and limits information available about temperature-dependent charge-carrier density and factors influencing electronic conductivity in perovskites, so far [11].

We study the dark electronic conductivity in perovskite single crystals via temperature-dependent pulsed-voltage space-charge-limited current (PV SCLC) measurements [11,12]. During the PV SCLC measurement, the voltage pulse is short, such that the induced ion motion is minimized and the waiting time between subsequent voltage pulses is sufficient for the system to relax back to its initial conditions after every bias pulse. We note that, even though we overcome, and hence do not need to account for, the influence of mobile ions, the presence of static ionic charge density still strongly influences the current-voltage characteristics, and is hence accounted for in our characterization and subsequent modeling [11].

Despite the fact that more accurate numerical approaches are available [13–17], the current density-voltage (J-V) curves for a semiconductor with traps, extracted from SCLC measurements, are typically subdivided into three distinct regions, if a number of assumptions, which we

---

[*] l.j.a.koster@rug.nl
[†] jclim@cnu.ac.kr
[‡] henry.snaith@physics.ox.ac.uk

discuss below, are valid. First is the Ohmic regime (1), where the current rises linearly with the voltage. For a semiconductor with a charge-carrier concentration n, Ohm's law is given by

$$J = \sigma E = en\mu \frac{V}{L}, \tag{1}$$

where $\sigma = en\mu$ is the electronic conductivity; μ is the charge-carrier mobility; e is the electronic charge; and E is the electric field, which is equal to V/L, where V is the applied voltage and L is the device thickness. We give an overview of all abbreviations used in this work in Table SI within the Supplemental Material [18]. Conventionally, Ohm's law is only valid if the thickness of the semiconductor is more than double the Debye length, such that the current is only driven by the drift of charge carriers [15]. If this is not the case, and the space-charge region from both contacts overlap, the overall charge density is increased. The low-voltage current density then follows the "moving electrode" equation rather than Ohm's law, and the departure from Ohm's law is thickness independent and occurs at around 0.9 V [15,19–22]. We report the moving electrode equation and the derivation of the crossover point in Table SII within the Supplemental Material [18]. After region (1), there is a so-called onset voltage after which the slope, $r = (d\ \log J)/(d \log V)$, in the J-V curve is larger than two due to the filling of trap states (2). It is important to note that this region will only occur if the traps are negatively charged when filled with an electron, and we elaborate on this point in the Simulation section of the Supplemental Material [18,23,24]. Under certain specific conditions [11,13,25], the number of trapped carriers in the material can be calculated from this onset voltage. However, numerical calculations have previously shown that ions, which are likely to exist in perovskites, contribute to the space charge in the bulk of the crystal, and thereby effectively negate the charge of trapped electrons [11]. Additionally, due to the soft nature of the perovskite material, it is very likely that traps are induced with thermal energy. Therefore, extracting the trapped carrier density via the onset voltage is rather complicated. Lastly, when all traps are filled, the drift current-density profile for a single carrier device is assumed to follow the Mott-Gurney law (3), where the current density is proportional to the voltage squared [26]. Röhr *et al.* show that there is only a very limited number of cases where the conductivity and mobility can be determined by evaluating the Mott-Gurney law at high voltages and Ohm's law at low voltages [15].

Here, we grow and compare methylammonium lead tribromide ($MAPbBr_3$) and methylammonium lead triiodide ($MAPbI_3$) single crystals of various thicknesses, and we show via temperature-dependent PV SCLC measurements that, for both crystal types, we observe a decrease in conductivity in regime (1) and an increase in onset voltage and slope in region (2) upon reducing the temperature. The experimental methods are discussed in the Supplemental Material [18,24,27,28].

Via both experiments and simulations, we provide a detailed insight into how a combination of multiple factors, including injection barrier, temperature-induced trap states, and ionic species, and a change in mobility, can affect the J-V curves. We note that this complicates the use of space-charge-limited current theory, and we present the use of drift-diffusion modeling for data analysis to extract important parameters from J-V characteristics in a mixed ionic and electronic systems.

We study both $MAPbBr_3$ and $MAPbI_3$ single crystals, where the screening effects of migrating ions on electrical conductivity are diminished by temperature-controlled PV SCLC measurements. Via PV SCLC measurements, we show that the background carrier density in single-crystal perovskites can be explained by a variety of factors that induce thermionic emission. An awareness and understanding of the charge-carrier density is very useful knowledge for the further development of device performance.

II. RESULTS

A. Intrinsic carrier density

First, we discuss the carrier density in an intrinsic semiconductor in which the Fermi level, E_F, lies in the middle of the band gap. In Fig. S1 within the Supplemental Material, we depict a simplified band diagram, the density of states, the Fermi-Dirac distribution at room temperature, and the carrier concentrations (from left to right) [18]. The intrinsic carrier-density electron density, n_i, in the conduction band, due to thermal population of carriers from the valence band, can be calculated using the following relation [29]:

$$n_i = \sqrt{N_C N_V} e^{-E_{\text{gap}}/2kT}, \tag{2}$$

where E_{gap} is the band-gap energy and N_C and N_V are the effective density of states in the conduction band and valence band, respectively, and are dependent on the effective electron and hole mass.

For $MAPbBr_3$, the effective electron mass, $m_{\text{eff},e}$, equals 0.234 m_e [30], such that N_C equals 2.77×10^{18} cm^{-3} at room temperature. For comparison, $MAPbI_3$ has an $m_{\text{eff},e}$ of 0.208 m_e [30], and therefore, N_C is 2.32×10^{18} cm^{-3} at room temperature. From this, and the 2.3- and 1.6-eV-wide band gap of $MAPbBr_3$ and $MAPbI_3$, respectively [30], we can calculate the thermal population of carriers in the conduction band as a function of temperature, as depicted in Fig. S2 within the Supplemental Material [18]. At room temperature, this would imply that, if perovskite single crystals were not extrinsically doped, their thermal population in the conduction band at room temperature would equal 6.00×10^{-2} and 4.09×10^{4} cm^{-3} for

$MAPbBr_3$ and $MAPbI_3$, respectively. Notably, N_C is proportional to $T^{1.5}$, and thus, only changes by slightly more than one order of magnitude over a temperature range from 50 to 2000 K. The community is, however, often under the wrong assumption that the extracted background carrier density in the low-voltage regime (1) is the intrinsic carrier density, which is explicitly the thermal population from the valence band.

B. Pulsed-voltage space-charge-limited current measurement

We perform temperature-dependent PV SCLC measurements and show the J-V characteristics of both $MAPbBr_3$ and $MAPbI_3$ single crystals in Figs. 1(a) and 1(b), respectively. We show similar trends for multiple thicknesses in Figs. S3a,b and S4a,b within the Supplemental Material for $MAPbBr_3$ and $MAPbI_3$, respectively [18]. We summarize all device types, dimensions, and their respective properties in Table SIII within the Supplemental Material [18]. Because $MAPbBr_3$ undergoes its first phase transition from cubic to tetragonal at around 220 K, we vary the temperature from 335 to 235 K [31]. For $MAPbI_3$, we can go to slightly lower temperatures (195 K), as it transitions from the tetragonal to orthorhombic phase at around 160 K [32]. For both crystals, we change the temperature in steps of 20 K, and we identify the characteristics of the J-V curve that are most influenced by temperature. In Fig. 1(c), we show a schematic indicating the three different regions in the J-V characteristics that occur upon lowering the temperature: (1) represents the decrease in the low-voltage Ohmic regime, (2) indicates the shift in the onset voltage towards lower voltages upon reducing the temperature, and (3) represents the increase in the slope of the J-V curve at voltages larger than the onset voltage. We elaborate upon these different regions in Secs. II C–E.

C. Background carrier density

From the Ohmic region in the J-V curves (region 1), we estimate a dark dc conductivity of $(1.02 \pm 0.03) \times 10^{-7}$ Sm^{-1} for a 160-μm-thick $MAPbBr_3$ crystal and $(4.43 \pm 0.98) \times 10^{-7}$ Sm^{-1} for a 280-μm-thick $MAPbI_3$ crystal at room temperature. Via transient photoconductivity measurements (TPC) [33], we extract a sum of mobilities at room temperature of (27 ± 1) $\mathrm{cm}^2/\mathrm{Vs}$ in $MAPbBr_3$ and (45 ± 3) $\mathrm{cm}^2/\mathrm{Vs}$ in $MAPbI_3$ (see Fig. S5 within the Supplemental Material [18]). We here assume that the electron and hole mobility are similar. It has been previously shown that the Hall mobility exhibits an inverse power-law temperature dependence in the cubic phase. Using the power exponent, $\mu \propto T^{-1.5}$ [34–36], we calculate the mobility values of the $MAPbBr_3$ crystals at all measured temperatures, with respect to our room-temperature-measured mobility. By applying Eq. (1), we determine n to be equal to 4.76×10^8 cm^{-3} for $MAPbBr_3$ and 1.24×10^9 cm^{-3} for $MAPbI_3$ at room temperature. We show in Fig. 2 that the background carrier density is orders of magnitude higher than the intrinsic carrier density (solid lines) calculated from thermodynamics. Using $\mu \propto T^{-1.5}$, we determine the carrier density at all measurement temperatures and we plot this in Fig. 2. We observe an expected increase in carrier density with increasing temperature, as shown by

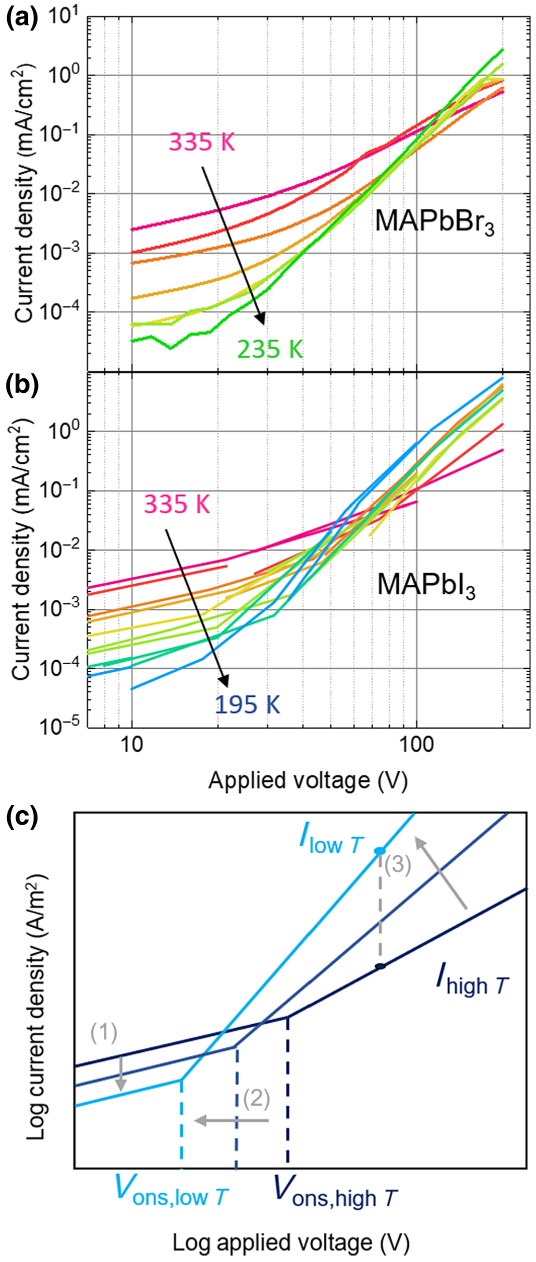

FIG. 1. Temperature-dependent PV SCLC measurements of (a) $MAPbBr_3$ (335 to 235 K in steps of 20 K) and (b) $MAPbI_3$ (335 to 195 K in steps of 20 K). (c) Schematic of J-V characteristics of the temperature-dependent PV SCLC measurement, where region (1) indicates the decrease in conductivity; region (2) is the shift of the onset voltage; and region (3) is the increase in slope in the trap-filling regime upon decreasing the temperature.

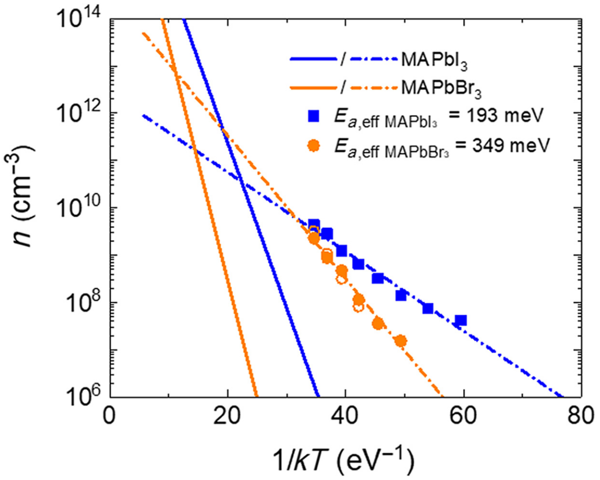

FIG. 2. Carrier density in the conduction band as a function of the reciprocal temperature for $\mathrm{MAPbBr_3}$ (orange) and $\mathrm{MAPbI_3}$ (blue). Solid lines indicate the intrinsic carrier density calculated from Eq. (2). Solid circles and squares are carrier densities estimated from experimental conductivity measurements. From this Arrhenius relationship, extrinsic carrier density in the conduction band is calculated, as indicated by the dashed lines. Numerical simulations (open circles) show carrier density in the bulk of the $\mathrm{MAPbBr_3}$ single crystal (far away from the charge-injection electrodes).

the solid circles and squares. From this Arrhenius relation, we extract an effective activation energy ($E_{a,\mathrm{eff}}$) of (349 ± 10) meV for $\mathrm{MAPbBr_3}$ and (193 ± 12) meV for $\mathrm{MAPbI_3}$. Notably, this effective activation energy is much higher than that of, for example, doped silicon, where the low ionization energy of ionizable donor or acceptor states is usually very close to the band edge. We elaborate on the processes governing this Arrhenius relation with the help of drift-diffusion simulations in Sec. II E. The dashed lines in Fig. 2 represent the calculated carrier density in the conduction band, extracted from conductivity data, as a function of the reciprocal temperature. These results clearly show that, over the temperature range of our measurements, we are far away from the intrinsic range and that the carrier density in the conduction band is governed by other processes that are discussed in Sec. II E.

D. Ionic space charge and trap states

We observe a departure from the Ohmic regime at the onset voltage, and we show in Fig. S6a within the Supplemental Material that this onset voltage shifts towards lower values upon reducing the temperature [18]. Additionally, there is a linear relation between the slope (r) of the log(J)-log(V) characteristics of the trap-filling regime as a function of temperature, as depicted in Fig. S6b within the Supplemental Material [18]. We show the variation of n, V_{ons}, and r for $\mathrm{MAPbBr_3}$ and $\mathrm{MAPbI_3}$ crystals of different thicknesses in Figs. S3c-e and S4c-h within the Supplemental Material, respectively [18]. Conventionally, it is assumed that the J-V characteristics start to deviate from being linear when the injected electrons are significantly filling the defect states in the band gap, and the slope with which the current density increases after the onset voltage can be used to determine the trap distribution [37,38]. However, we have previously shown that, if the density of ionic space charge (which is static) is within the same order of magnitude as that of the density of defect states, the onset voltage shifts and the slope is affected, thereby making it ambiguous to quantitatively describe the change in slope and extract the trap density from the onset voltage [11].

E. Drift-diffusion simulations

To pinpoint which effects govern the higher-than-expected intrinsic charge-carrier density, the effective activation energy, and the change in V_{ons} and r, we numerically simulate the J-V characteristics using a one-dimensional drift-diffusion model that includes electrons and holes as well as ionic species (notably, the ionic species are static for our simulations). Le Corre *et al.* have recently demonstrated that drift diffusion simulation can accurately reproduce PV SCLC J-V curves, which will be published elsewhere. Here we employ this modeling methodology to extract trap and ion densities, and mobility over a range of temperature. See the simulation part within the Supplemental Material for details on our device model [18,39–43]. The simulation mimics the pulsed-voltage measurements by first calculating the ionic distribution at 0 V, and then sweeping the voltage, while keeping the ions fixed. In this way, the current-voltage measurements are recreated without redistributing the mobile ions through the crystal.

We first fit the dark J-V curve at room temperature, as shown in Fig. S8a within the Supplemental Material [18], from which we extract an electron mobility of 12.9 cm^2/Vs, a trap density (N_{trap}) of 1.52×10^{13} cm^{-3}, and an ion density (N_{ion}) of 3.19×10^{12} cm^{-3}. This mobility is in very close agreement with the sum of mobilities we determine from the TPC measurement (26.8/2 = 13.4 cm^2/Vs). We find that we can only fit the experimental data by implementing an injection barrier (E_{barrier}), due to misalignment of the work functions of the contact and the conduction band of the perovskite, where the electron density at the contact (n_{contact}) is given as follows:

$$n_{\mathrm{contact}} = N_c e^{-E_{\mathrm{barrier}}/kT} . \tag{3}$$

Then, at any given temperature, there will be a number of carriers that flow freely into the material to equilibrate the Fermi levels due to thermionic-emission-controlled injection. Without this barrier, our simulated current density is orders of magnitude larger than the experimentally measured current density. The device parameters for the room

TABLE I. Summarized extracted values from numerical modeling of the J-V curve of 160-μm-thick $MAPbBr_3$ single crystal at room temperature.

Property	Value
Mobility	$12.9\ cm^2/Vs$
Trap density	$1.52 \times 10^{13}\ cm^{-3}$
Ion density	$3.19 \times 10^{12}\ cm^{-3}$
Carrier density	$3.17 \times 10^{8}\ cm^{-3}$

temperature fit are given in Table SV within the Supplemental Material [18]. We stress that, because the ion and trap density are within the same order of magnitude, the sharp onset expected for SCLC measurements is softened, an effect that we have previously described [11]. Additionally, we simulate the carrier density in the bulk of the $MAPbBr_3$ single crystal, as shown by the open circles in Fig. 2, and we find that this is in good agreement with the values extracted from fitting Ohm's law to region (1). We report the extracted free carrier density and trap and ion densities as a function of position in the $MAPbBr_3$ crystal in Fig. S9 within the Supplemental Material [18] and summarize the values in the middle of the crystal, as determined from room-temperature simulations, in Table I.

We then fit the temperature-dependent J-V characteristics, as shown in Fig. 3. To do this, we have to account for several input parameters that change with temperature. First, we vary the mobility with temperature, basing it on our measured room-temperature value and assuming the power law $\mu \propto T^{-1.5}$, which has been observed previously in other metal-halide perovskites, such as $MAPbI_3$ [43]. We also vary the density of states as $N_C \propto T^{1.5}$ and the thermionic carrier injection following Eq. (3). Additionally, we take into account the soft nature of the perovskite material, and we vary the trap density with temperature via $N_{\mathrm{trap}} = N_{\mathrm{trap},0}e^{-E_{a,\,\mathrm{trap}}/kT}$, where $N_{\mathrm{trap},0}$ is the trap-density value extracted from the numerical fit at room temperature, and $E_{a,\mathrm{trap}}$ is the activation energy with which traps are induced as the temperature rises. The model also accounts for the equilibrium between free and trapped carriers, which varies with temperature. We extract the ratio between ion and trap density at room temperature and, for simplicity, keep this ratio constant at different temperatures, which appears to accurately reproduce the experimental results. Our assumption here is that the ions and traps are related in some manner. As can be seen in Fig. 3, we observe good agreement between experimental and simulation data.

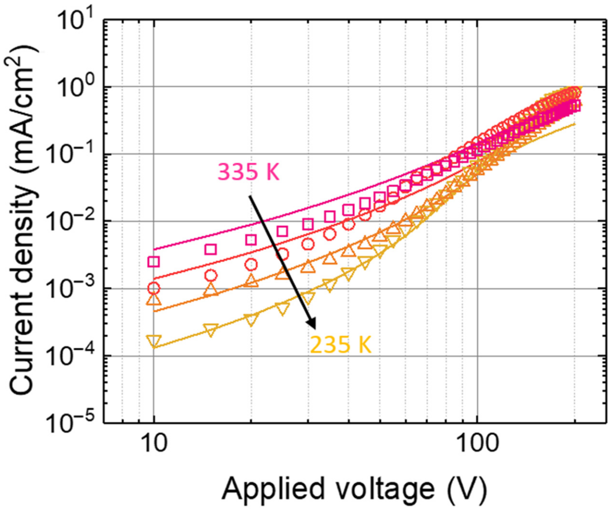

FIG. 3. Simulated current-voltage characteristics (solid lines) of temperature-dependent PV SCLC measurements (scattered lines) for 160-μm-thick $MAPbBr_3$ single crystal.

We give additional information on the temperature-dependent simulations in the Supplemental Material [18]. We first show in Fig. S8b within the Supplemental Material that the conductivity increases with temperature in the low-voltage regime due to thermionic injection from the contact and thermal population from trapped carriers [18]. Second, we show by simulation of the J-V curves with a fixed mobility for all temperatures, in Fig. S8c within the Supplemental Material [18], that the effect of reduced mobility with increasing temperature is strongly overshadowed by the thermal increase in carrier density.

We note that the increase in trap and ion densities and decrease in mobility with increasing temperature influences the overall changes in conductivity with temperature in the opposite manner to the effect of increasing carrier density due to thermionic emission from the contact and the traps.

With this study, we emphasize that the fraction of free carriers in the system is governed by a combination of mechanisms that cannot be disentangled from each other via a single J-V measurement. Therefore, we stress that, from dark-conductivity-extracted activation energies are effective activation energies ($E_{a,\,\mathrm{eff}}$), and that these are mainly governed by the temperature-dependent density of traps and ions, temperature-dependent charge-carrier mobility (both causing a decrease in conductivity with increasing temperature), and the injection barrier and ionization of trapped carriers (causing an increase in free-carrier density with increasing temperature). Overall, our model comprising these factors well describes temperature-dependent PV SCLC data. Although some deviations can originate from the fact that we have assumed that the mobility varies with temperature as $\mu \propto T^{-1.5}$, which is the case where the mobility is entirely governed by phonon scattering, scattering from defects may also be a contributing factor, which would lead to a slightly different temperature dependence [43]. Additionally, there may be a contribution to the thermal population of carriers from ionizable impurity donor or acceptor sites, which we do not include in our model beyond the presence of ionizable traps.

From the PV SCLC measurements at different thicknesses, we find an average effective activation energy, which is independent of thickness, of (333 ± 26) meV for $MAPbBr_3$ and (217 ± 21) meV for $MAPbI_3$. The intrinsic conductivity increases more steeply with a lower band gap, and the extrinsic conductivity increases more steeply due to a lower barrier for thermionic emission, shallower traps, different temperature-dependent mobility, and different activation energy for trap generation.

III. CONCLUSION

We provide a detailed investigation into the changes in dark J-V characteristics of metal-halide perovskite single crystals with changing temperature, and we reveal electronic processes that affect the conductivity in these perovskite crystals. We do this via PV SCLC measurements, which account for the presence of static ionic charge, but overcome the issue of having to deconvolute the influence of the movement of these ions, in combination with numerical modeling. We envision that knowledge of these characteristic properties will be of great importance for understanding the combined ionic and electronic conductivity in perovskites. We perceive that combining our findings here with other investigations on the influence of mobile ions, such as transient-ion-drift and impedance spectroscopy, will lead to a better understanding of the nature of the defects and the combined ionic and electronic properties of metal-halide perovskites and devices.

ACKNOWLEDGMENT

This project is funded by the Engineering and Physical Sciences Research Council (EPSRC), Grants No. EP/M005143/1 and No. EP/S004947/1. E.A.D. thanks the EPSRC for funding via the Centre for Doctoral Training in New and Sustainable Photovoltaics. The work by V.M.L.C. is supported by a grant from STW/NWO (VIDI 13476).

E.A.D. and J.L. fabricated the devices, performed experiments, and analyzed data. V.M.L.C. and L.J.A.K. performed simulations and analyzed data. All authors discussed the results and reviewed the manuscript. J.L. and H.J.S. guided and supervised the overall project.

H.J.S. is cofounder and CSO of Oxford PV Ltd., a company commercializing perovskite PV technology.

[1] A. Kojima, K. Teshima, Y. Shirai, and T. Miyasaka, Organometal halide perovskites as visible-light sensitizers for photovoltaic cells, J. Am. Chem. Soc. **131**, 6050 (2009).

[2] M. M. Lee, J. Teuscher, T. Miyasaka, T. Murakami, and H. J. Snaith, Efficient hybrid solar cells based on meso-superstructured organometal halide perovskites, Science **338**, 643 (2012).

[3] Best Research-Cell Efficiency Chart | Photovoltaic Research | NREL. Available at: https://www.nrel.gov/pv/cell-efficiency.html. (Accessed: 12th August 2020)

[4] H. Zhum Y, Fum F. Meng, X. Wu, Z. Gong, Q. Ding, M. V. Gustafsson, M. Trinh, S. Jin, and X. Y. Zhu, Lead halide perovskite nanowire lasers with low lasing thresholds and high quality factors, Nat. Mater. **14**, 636 (2015).

[5] G. Xing, N. Mathews, S. S. Lim, N. Yantara, X. Liu, D. Sabba, M. Gratzel, S. Mhaisalkar, and T. C. Sum, Low-temperature solution-processed wavelength-tunable perovskites for lasing, Nat. Mater. **13**, 476 (2014).

[6] Z. K. Tan, R. S. Moghaddam, M. L. Lai, P. Docampo, R. Higler, F. Deschler, M. Price, A. Sadhanala, L. M. Pazos, D. Credgington, *et al.*, Bright light-emitting diodes based on organometal halide perovskite, Nat. Nanotechnol. **9**, 687 (2014).

[7] V. B. Mykhaylyk, H. Kraus, and M. Saliba, Bright and fast scintillation of organolead perovskite $MAPbBr_3$ at Low temperatures, Mater. Horizons **6**, 1740 (2019).

[8] H. J. Snaith, A. Abate, J. M. Ball, G. E. Eperon, T. Leijtens, N. K. Noel, S. D. Stranks, J. T. W. Wang, K. Wojciechowski, and W. Zhang, Anomalous hysteresis in perovskite solar cells, J. Phys. Chem. Lett. **5**, 1511 (2014).

[9] D. Moia, I. Gelmetti, P. Calado, W. Fisher, M. Stringer, O. Game, Y. Hu, P. Docampo, D. Lidzey, E. Palomares, *et al.*, Ionic-to-electronic current amplification in hybrid perovskite solar cells: Ionically gated transistor-interface circuit model explains hysteresis and impedance of mixed conducting devices, Energy Environ. Sci. **12**, 1296 (2019).

[10] W. Tress, Metal halide perovskites as mixed electronic-ionic conductors: Challenges and opportunities - from hysteresis to memristivity, J. Phys. Chem. Lett. **8**, 3106 (2017).

[11] E. A. Duijnstee, J. M. Ball, V. M. Le Corre, L. J. A. Koster, H. J. Snaith, and J. Lim, Toward understanding space-charge limited current measurements on metal halide perovskites, ACS Energy Lett. **5**, 376 (2020).

[12] J.M. Ball, jmball/SCLC, first release (version v1.0.0). (2019), https://doi.org/10.5281/Zenodo.3369666.

[13] J. A. Röhr, X. Shi, S. A. Haque, T. Kirchartz, and J. Nelson, Charge Transport in Spiro-OMeTAD Investigated Through Space-Charge-Limited Current Measurements, Phys. Rev. Appl. **9**, 044017 (2018).

[14] J. A. Röhr, Direct Determination of Built-in Voltages in Asymmetric Single-Carrier Devices, Phys. Rev. Appl. **11**, 054079 (2019).

[15] J. A. Röhr, T. Kirchartz, and J. Nelson, On the correct interpretation of the low voltage regime in intrinsic single-carrier devices, J. Phys. Condens. Matter **29**, 205901 (2017).

[16] H. T. Nicolai, G. A. H. Wetzelaer, B. de Boer, C. Campbell, C. Risko, J. L. Bredas, and P. W. M. Blom, Unification of trap-limited electron transport in semiconducting polymers, Nat. Mater. **11**, 882 (2012).

[17] J. Dacuña, W. Xie, and A. Salleo, Estimation of the spatial distribution of traps using space-charge-limited current

measurements in an organic single crystal, Phys. Rev. B **86,** 115202 (2012).
[18] See the Supplemental Material at http://link.aps.org/supplemental/10.1103/PhysRevApplied.15.014006 for abbreviations, additional experimental and modeling results, methods, key equations, and modeling background.
[19] R. De Levie, N. G. Seidah, and H. Moreira, Transport of ions of One kind through thin membranes, J. Membr. Biol. **10**, 171 (1972).
[20] A. A. Grinberg and S. Luryi, Space-charge-limited current and capacitance in double-junction diodes, J. Appl. Phys. **61**, 1181 (1987).
[21] G. A. H. Wetzelaer and P. W. M. Blom, Ohmic current in organic metal-insulator-metal diodes revisited, Phys. Rev. B **89**, 241201 (2014).
[22] S. L. M. van Mensfoort and R. Coehoorn, Effect of Gaussian disorder on the voltage dependence of the current density in sandwich-type devices based on organic semiconductors, Phys. Rev. B **78**, 085207 (2008).
[23] I. E. Castelli, J. M. García-Lastra, K. S. Thygesen, and K. W. Jacobsen, Bandgap calculations and trends of organometal halide perovskites, APL Mater. **2**, 081514 (2014).
[24] F. Brivio, K. T. Butler, A. Walsh, and M. van Schilfgaarde, Relativistic quasiparticle self-consistent electronic structure of hybrid halide perovskite photovoltaic absorbers, Phys. Rev. B **89**, 155204 (2014).
[25] M. A. Lampert and P. Mark, *Current Injection in Solids* (Academic Press, New York, 1970).
[26] N. F. Mott and R. W. Gurney, *Electronic Processes in Ionic Crystals* (Oxford University Press, New York, 1940).
[27] P. Nayak, D. T. Moore, B. Wnger, S. Nayak, A. A. Haghighirad, A. Fineberg, N. K. Noel, O. G. Reid, G. Rumbles, P. Kukura, K. A. Vincent, and H. J. Snaith, Mechanism for rapid growth of organic–inorganic halide perovskite crystals, Nat. Commun. **7**, 13303 (2016).
[28] B. Wenger, P. Nayak, X. Wen, S. V. Kesava, N. K. Noel, and H. J. Snaith, Consolidation of the optoelectronic properties of $CH_3NH_3PbBr_3$ perovskite single crystals, Nat. Commun. **8**, 590 (2017).
[29] S. M. Sze and K. K. Ng, *Physics of Semiconductor Devices* (John Wiley & Sons, Inc., New York, 1969).
[30] K. Galkowski, A. Mitioglu, A. Miyata, P. PLochocka, O. Portugall, G. E. Eperon, J. T. W. Wang, T. Stergiopoulos, S. D. Stranks, H. J. Snaith, and R. J. Nicholas, Determination of the exciton binding energy and effective masses for methylammonium and formamidinium lead Tri-halide perovskite semiconductors, Energy Environ. Sci. **9**, 962 (2016).
[31] K. H. Wang, L. C. Li, M. Shellaiah, and K. Wen Sun, Structural and photophysical properties of methylammonium lead tribromide ($MAPbBr_3$) single crystals, Sci. Rep. **7**, 13643 (2017).
[32] P. S. Withfield, N. Herron, W. E. Guise, K. Page, Y. Q. Cheng, I. Milas, and M. K. Crawford, Structures, phase transitions and tricritical behavior of the hybrid perovskite methyl ammonium lead iodide, Sci. Rep. **6**, 35685 (2016).
[33] T. Leijtens, J. Lim, J. Teuscher, T. Park, and H.J. Snaith, Charge density dependent mobility of organic hole-transporters and mesoporous TiO_2 determined by transient mobility spectroscopy: implications to dye-sensitized and organic solar cells, Adv. Mater. **23**, 3227 (2013).
[34] L. M. Herz, How lattice dynamics moderate the electronic properties of metal-halide perovskites, J. Phys. Chem. Lett. **9**, 6853 (2018).
[35] H. T. Yi, X. Wu, X. Zhu, and V. Podzorov, Intrinsic charge transport across phase transitions in hybrid organo-inorganic perovskites, Adv. Mater. **28**, 6509 (2016).
[36] T. Savenije, C. S. Ponseca, L. Kunneman, M. Abdellah, K. Zheng, Y. Tian, S. E. Canton, I. Scheblykin, T. Pullerits, A. Yartsev, and V. Sundstrom, Thermally activated exciton dissociation and recombination control the carrier dynamics in organometal halide perovskite, J. Phys. Chem. Lett. **5**, 2189 (2014).
[37] P. Mark and W. Helfrich, Space-charge-limited currents in organic crystals, J. Appl. Phys. **33**, 205 (1962).
[38] A. Rose, Space-charge-limited currents in solids, Phys. Rev. **97**, 1538 (1955).
[39] T. S. Sherkar, C. Momblona, L. Gil-Escrig, H. J. Bolink, and L. J. A. Koster, Improving perovskite solar cells: Insights from a validated device model, Adv. Energy Mater. **7**, 1602432 (2017).
[40] T. S. Sherkar, C. Momblona, L. Gil-Escrig, J. Avila, M. Sessolo, H. J. Bolink, and L. J. A. Koster, Recombination in perovskite solar cells: Significance of grain boundaries, interface traps, and defect ions, ACS Energy Lett. **2**, 1214 (2017).
[41] V. M. Le Corre, M. Stolterfoht, L. Perdigon Toro, M. Feuerstein, C. Wolff, L. Gil-Escrig, H. J. Bolink, D. Neher, and L. J. A. Koster, Charge transport layers limiting the efficiency of perovskite solar cells: How To optimize conductivity, doping, and thickness, ACS Appl. Energy Mater. **2**, 6280 (2019).
[42] L. J. A. Koster, E. C. P. Smits, V. D. Mihailetchi, and P. W. M. Blom, Device model for the operation of polymer/fullerene bulk heterojunction solar cells, Phys. Rev. B **72**, 085205 (2005).
[43] L. M. Herz, Charge-Carrier mobilities in metal halide perovskites: Fundamental mechanisms and limits, ACS Energy Lett. **2**, 1539 (2017).